


## Hiding Images in Quantum Correlations

Chloé Vernière<sup>✉\*</sup> and Hugo Defienne<sup>✉</sup>

*Sorbonne Université, CNRS, Institut des NanoSciences de Paris, INSP, F-75005 Paris, France*

 (Received 5 March 2024; revised 30 May 2024; accepted 16 July 2024; published 29 August 2024)

Photon-pair correlations in spontaneous parametric down-conversion are ubiquitous in quantum photonics. The ability to engineer their properties for optimizing a specific task is essential, but often challenging in practice. We demonstrate the shaping of spatial correlations between entangled photons in the form of arbitrary amplitude and phase objects. By doing this, we encode image information within the pair correlations, making it undetectable by conventional intensity measurements. It enables the transmission of complex, high-dimensional information using quantum correlations of photons, which can be useful for developing quantum communication and imaging protocols.

DOI: [10.1103/PhysRevLett.133.093601](https://doi.org/10.1103/PhysRevLett.133.093601)

Spontaneous parametric down-conversion (SPDC) is the source for many quantum optics experiments. In such a nonlinear process, a photon from the pump beam spontaneously splits into two entangled photons of lower frequencies. At the outputs, properties of down-converted photons are set by the type and geometry of the nonlinear crystal, and the pump beam characteristics [1]. The ability to engineer these properties is key for quantum photonics applications.

Many techniques have been developed to control correlations and entanglement of down-converted photons. Engineering the crystal parameters, such as its poling profile and overall geometry, allows, for example, to control spectral and spatial properties of the pairs [2–4]. Another well-established way to manipulate their properties is to shape the pump beam. Although a few works report on spectral correlation control [5,6], the majority focus on manipulating spatial correlations between photon pairs by modulating the pump’s spatial profile. This is typically done using spatial light modulators (SLMs). Experimental demonstrations involve structuring the pump in the form of discrete spatial modes carrying orbital angular momentum (OAM) to influence correlations in the corresponding bases [7–14], modulating its spatial phase in the crystal plane to engineer momentum correlations [15–17], controlling its spatial coherence to tune the degree of entanglement [18,19], and even actively compensating for scattering [20].

Using SLMs, however, the complexity of the correlation structures that can be generated is limited. Interestingly, two studies conducted in different contexts—one to study coherence transfer [21] and the other to investigate spatial resolution enhancement [22]—have indirectly modulated correlations between pairs without using a SLM but placing

simple amplitude objects in the pump path. In our work, we generalize this concept and demonstrate that momentum correlations can be shaped under the form of arbitrary amplitude and phase objects. By doing so, images are encoded in the correlations between photons and are not detectable by conventional intensity measurements.

Our approach is based on a key property of SPDC, which involves the complete transfer of the pump’s spatial coherence to that of the down-converted field [23]. As shown in Fig. 1(a), photon correlations are shaped by projecting the Fourier spectrum of a given object  $t$  onto a thin nonlinear crystal. The down-converted field produced in the crystal plane has a transverse spatial shape identical to that of the object’s Fourier transform. After the crystal, it propagates as a spatially incoherent field, leading to an intensity  $I$  that remains flat and constant in the far field [Fig. 1(b)]. By looking at the second-order coherence, however, the correlation function is

$$G^{(2)}(\mathbf{r}_-, \mathbf{r}_+) = \left| t\left(-\frac{f}{f'}\mathbf{r}_+\right) \right|^2, \quad (1)$$

where  $f$  (resp.  $f'$ ) are the focal lengths of the lenses before (resp. after) the crystal,  $\mathbf{r}_- = \frac{1}{2}(x_1 - x_2, y_1 - y_2)$  and  $\mathbf{r}_+ = \frac{1}{2}(x_1 + x_2, y_1 + y_2)$  are defined as the minus and sum coordinates, respectively, and  $x_1, y_1, x_2$  and  $y_2$  are the transverse spatial coordinate associated with each photon. To reveal the object, one can measure  $G^{(2)}$  and sum it along the minus-coordinate axis, i.e.,  $\Gamma^+(\mathbf{r}_+) = \int G^{(2)}(\mathbf{r}_-, \mathbf{r}_+) d\mathbf{r}_- \propto |t(\mathbf{r}_+)|^2$ . For clarity,  $\Gamma^+$  will be referred to as the “correlation image” throughout the Letter. Figure 1(c) shows such a correlation image revealing the standing-cat shaped object. In the following, we provide a comprehensive description of the experimental system used to capture these images. Additionally, we conduct an in-depth analysis of our approach, assessing its

\*Contact author: [chloe.vernierre@insp.jussieu.fr](mailto:chloe.vernierre@insp.jussieu.fr)

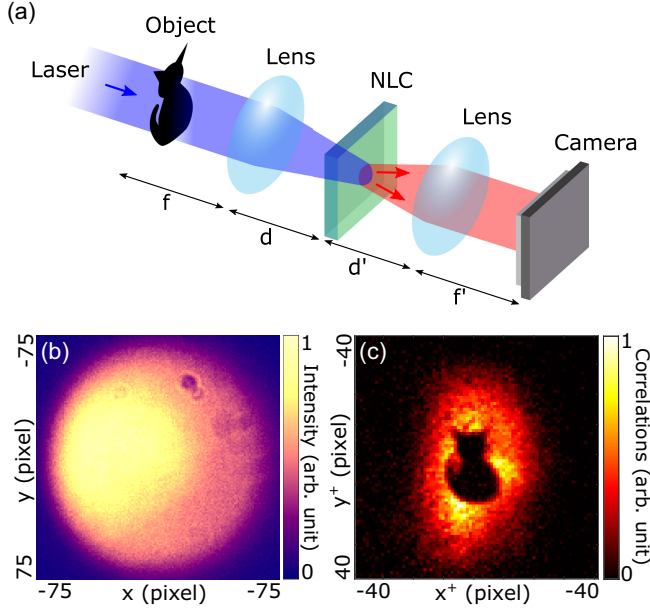


FIG. 1. Encoding images in photon correlations. (a) Simplified experimental scheme. A continuous wave laser at 405 nm illuminates an object (standing cat-shaped mask). It is Fourier imaged onto a thin nonlinear crystal (NLC) by a lens  $f$ . Spatially entangled photon pairs produced by spontaneous parametric down-conversion (SPDC) around 810 nm are detected in a Fourier plane of the crystal using a lens ( $f'$ ) and a single-photon sensitive camera. The distance between the object and the first lens, and this between the second lens and the camera must be set to  $f$  and  $f'$ , respectively.  $d \neq f$  and  $d \neq f'$  in general. (b) Conventional output intensity image  $I(x, y)$ . (c) Sum-coordinate projection  $\Gamma^+(x^+, y^+)$  of the second-order spatial correlation function  $G^{(2)}$ , referred to as the “correlation image.”  $9 \times 10^6$  frames were acquired using an Electron Multiplied Charge Couple Device (EMCCD) camera and with the specific lenses’ arrangements detailed in Fig. 2(a), and Fig. S1 of [24].

compatibility with both phase and amplitude objects, the flexibility of its setup, and the quality of the resulting correlation image.

A more detailed experimental setup is shown in Fig. 2(a). An amplitude object is illuminated by a blue collimated laser beam at 405 nm. The object is then Fourier-imaged onto a 1 mm-thick  $\beta$ -barium borate (BBO) crystal. Degenerate spatially entangled photon pairs at 810 nm are produced via type-I SPDC. At the output, the crystal plane is Fourier-imaged onto an Electron Multiplied Charge Coupled Device (EMCCD) camera by  $f'$  and further magnified by  $f_1$ - $f_2$ , allowing photons momenta to be matched to pixel positions. The EMCCD camera is used to perform both intensity and correlations measurement between the incident photons, enabling the computation of  $I$  and  $G^{(2)}$  for the photons pairs using the method described in Ref. [25].

Figures 1(b) and 1(c) show intensity and correlation images, respectively, obtained using an opaque mask of a

standing cat as the object. Similar results are also obtained using a transparent mask with a sleeping cat shape, as shown in Fig. 3(a). In both cases, the objects are not visible in the direct intensity images; they can only be unveiled through correlation measurements. Additionally, imaging the crystal surface does not allow us to retrieve the object (see Sec. VIII of the Supplemental Material [24]). This “hiding” of images within photon correlations becomes even more noticeable when the intensity of the photon pair beam is also spatially modulated. For example, one can insert a second object, such as a mask shaped like a standing cat, positioned at the center of the photon pair beam path, within a Fourier plane between  $f'$  and  $f_1$ . In this case, an intensity measurement reveals an image of the standing cat mask [Fig. 3(b), inset], while a correlation measurement reveals that of the sleeping cat [Fig. 3(b)].

Our approach also operates with phase objects. To demonstrate this, we use a pointlike object, i.e.,  $t(\mathbf{r}) \approx \delta(\mathbf{r})e^{i\theta_t(\mathbf{r})}$ , where  $\theta_t$  is its phase and  $\delta$  the Dirac delta function. It is visible in the correlation image shown in Fig. 3(c). In practice, this object is virtual. It is created by removing the lens  $f$  from the experimental setup in Fig. 2(a). Indeed, by doing so, the laser illuminating the crystal becomes collimated, equivalent to imaging a pointlike object with a width inversely proportional to the beam diameter. Then, a glass slide (microscope slide) is inserted into the pump beam path to set its phase  $\theta_t$  to a random arbitrary value.

To retrieve the phase, a common-path interferometer is constructed. Modifications to the experimental setup are shown in Fig. 2(b). The collimated pump beam is divided into two optical paths using a half wave plate (HWP) at  $22.5^\circ$  and two beam displacers (BDs). The microscope slide is placed in one of the paths (the imaging path) while the other is used as a reference. A second type-I BBO crystal is added to the setup. It is optically contacted to the first one and rotated  $90^\circ$ . This second crystal interacts with the reference pump to produce photon pairs that are cross-polarized to those generated by the first crystal. Both down-converted fields are Fourier-imaged and superimposed onto the camera. To make them interfere, the polarizer is rotated to  $45^\circ$ . In addition, a SLM is placed between lenses  $f_1$  and  $f_2$  (not represented). It allows us to control the phase  $\theta$  of the vertically polarized photon pairs, i.e., those generated by the reference pump.

In the camera plane, the second-order correlation function can thus be written

$$G^{(2)}(\mathbf{r}_-, \mathbf{r}_+) = |t(\mathbf{r}_+) + e^{i2\theta}|^2 \propto |\cos[\theta_t(\mathbf{r}_+) - 2\theta]|^2, \quad (2)$$

where the magnification factor has been omitted for clarity.  $\theta_t$  is reconstructed by acquiring  $G^{(2)}$  for four different phase shifts  $\theta \in [0, \pi/4, \pi/2, 3\pi/4]$  using the phase-shifting holography formula [26]. Figure 3(d) shows an image of the object’s phase. In the region where it is correctly

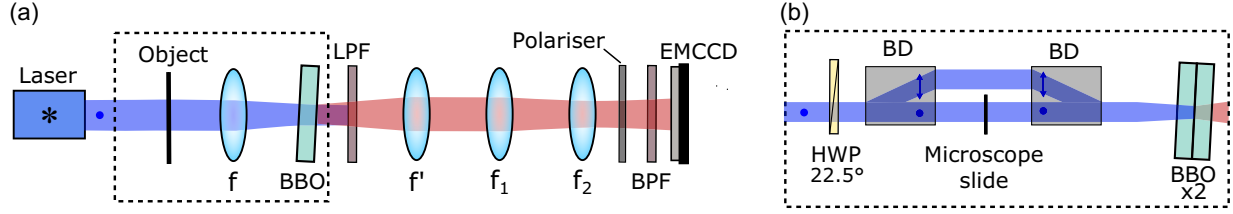


FIG. 2. Experimental setup. (a) For imaging amplitude objects, a continuous wave laser emits a collimated beam of horizontally polarized light at  $\lambda_p = 405$  nm. The beam with a diameter of approximately 2 mm illuminates an amplitude object. The object is positioned in the focal plane of lens  $f$  which focuses the beam into a 0.5 mm thick nonlinear crystal of  $\beta$ -barium borate (BBO). Within this crystal, photons at 405 nm undergo type-I SPDC, transforming into degenerate spatially entangled photons at 810 nm. A long-pass filter (LPF) filters out the pump beam after the crystal. The generated photons are collected by the lens  $f' = 35$  mm and pass through lenses  $f_1$  and  $f_2$ . An EMCCD camera positioned in the focal plane of  $f_2$  detects the photons. A bandpass filter (BPF) at  $810 \pm 5$  nm and a vertically positioned polarizer eliminate pump residues and ambient light. They also improve the strength of spatial correlations by filtering the spatio-spectral coupling in the SPDC cone. The distance between each consecutive lens is equal to the sum of each lens's focal length. (b) For phase imaging, all the elements located in the black dashed line box are replaced by an interferometric system. A half wave plate (HWP) at  $22.5^\circ$  is positioned after the laser. Two beam displacers (BDs) in calcite are placed in succession to create the two arms of the interferometer, in one of which a microscope slide is inserted to shift the phase. The polarizer before the camera is set to  $45^\circ$ . A spatial light modulator (SLM) is inserted in the focal plane between lenses  $f_1$  and  $f_2$  (not represented). See also Secs. I and IV of [24] for more details on the experimental setups.

defined (amplitude  $> 2\%$  maximum), we observe that the phase is not perfectly uniform due to the spatial phase inherent to the imaging system. To remove it, we subtract this phase image by a reference phase image acquired without the presence of the object. We obtain Fig. 3(e) that is more uniform, albeit noisier. A reference arm is not fundamentally needed to encode a phase object. It is only used here to confirm phase encoding through a phase-shifting interference technique, previously used in Refs. [27,28]. Alternative methods like transport of intensity equation [33] and pump interferometry [34] can also be employed. Section IV of [24] details the phase-shifting process.

Finally, we analyze some practical aspects of our approach, including the flexibility of its optical arrangement and the trade-off between spatial resolution and signal-to-noise ratio (SNR). As pointed out in Fig. 1(a),

the distance  $d$  between lens  $f$  and the crystal, and the distance  $d'$  between the crystal and lens  $f'$ , are not constraints. Indeed, it can be shown theoretically that when  $d$  and  $d'$  differ from  $f$  and  $f'$ , respectively, only an extra phase term is produced on the down-converted field in the camera plane, that is not detected by correlation measurement (see Sec. V of [24]). Experimentally, Figs. 4(a)–4(c) show three correlation images obtained using the configuration illustrated in Fig. 2(a). However, in this case, a vertical line of a line resolution target was employed as the object and we used different values of  $d$  and  $d'$ . We observe nearly identical images, verifying in practice the theory that the distances between the lenses and the crystal are irrelevant. This is further confirmed by the profiles in Fig. 4(d).

Furthermore, Fig. 5 shows the variations in spatial resolution and SNR in the correlation image as a function

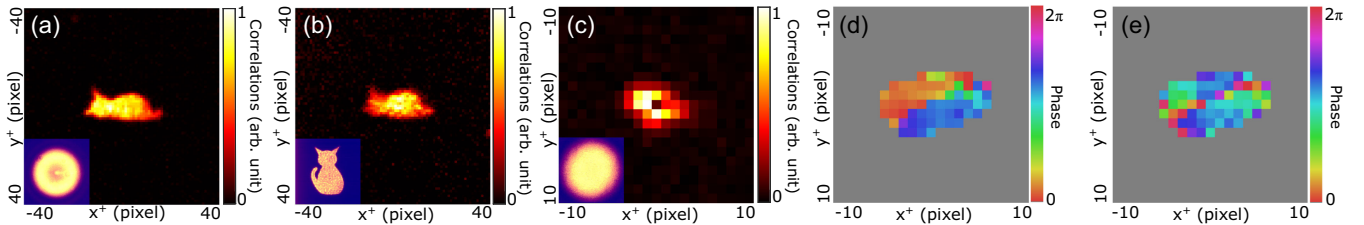


FIG. 3. Results with amplitude and phase objects. (a),(b) Correlation images obtained using a sleeping-cat-shaped mask as the object. The inset at the bottom left shows the intensity image.  $3.8 \times 10^6$  and  $6.3 \times 10^6$  frames were acquired. (b) We also insert a second object with a standing cat shape in the photon pair beam path. This second object was inserted in the Fourier plane between lenses  $f_1$  and  $f_2$  shown in Fig. 2(a). (c) Correlation image revealing the amplitude shape of a virtual pointlike object after the phase-shifting process. We observe that, due to aberrations in the imaging system, its shape is not perfectly Gaussian. (d) Measured phase with the object, reconstructed by phase-shifting holography. The gray area corresponds to undefined phases where the amplitude of the correlations is below 2% of their maximum value.  $10^7$  frames were acquired. (e) Phase of the object after subtraction of the reference phase acquired without the object.

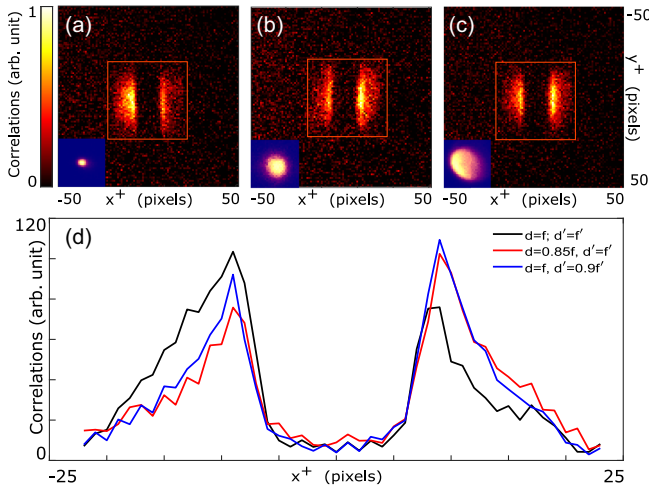


FIG. 4. Distance independence. Correlation measurements acquired while varying the distances  $d$  and  $d'$  such that (a)  $d = f$ ,  $d' = f'$ ; (b)  $d = 0.85f$ ,  $d' = f'$ ; (c)  $d = f$ ,  $d' = 0.9f'$ . The object imaged is one vertical line of a line grating resolution target. (d) Correlation intensity profile vertically averaged in the region inside the red square in (a)–(c). The insets at the bottom left show the intensity images obtained by imaging the crystal surface. They demonstrate that a significant defocus is being introduced between the configurations in (a) and (b),(c).  $6.6 \times 10^5$  frames were acquired for each correlation image and each inset image has a size of  $31 \times 31$  pixels.

of the focal length  $f$ . In this context, we refer to the spatial resolution as pixel resolution, i.e., the total number of pixels over which the image is discretized. It corresponds to the width of the illumination area measured in a correlation image without any object present. The blue curve (left

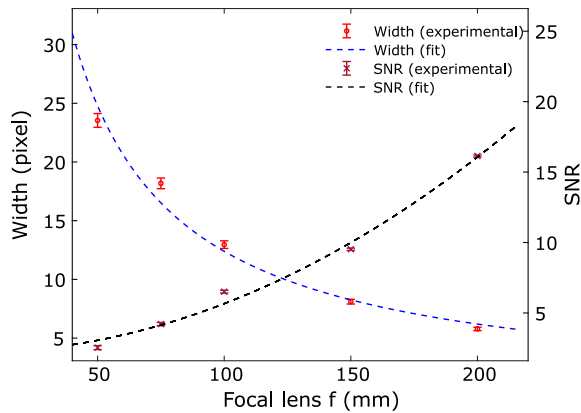


FIG. 5. Signal-to-noise ratio (SNR) and resolution trade-off. Left scale: correlation width as a function of the focal length  $f$ . Experimental data (red circles) and fit (dashed blue).  $6.6 \times 10^5$  frames were acquired for all data points, except for  $f = 50$  mm for which  $5 \times 10^6$  frames were required. Fit according to a  $1/f$  relationship as predicted by the theory model. Right scale: SNR (dark red crosses) and fit (dashed black) as a function of the focal length  $f$ . Fit according to a  $f^2$  relationship.  $6.6 \times 10^5$  frames were acquired for each data point.

scale) shows the resolution of the system for different lenses  $f$  of focal lengths 50, 75, 100, 150, and 200 mm. The smaller the focal length  $f$  is, the wider is the correlation width, with a  $1/f$  relationship [35]. However, as shown by the black curve (right scale), decreasing  $f$  also deteriorates the SNR in the retrieved image (for a fixed acquisition time), which evolves as  $f^2$ . There is thus a trade-off between the image pixel resolution and its SNR.

**Conclusion**—We have demonstrated the shaping of quantum correlations between photon pairs into amplitude and phase objects. During SPDC, the first-order spatial coherence of the pump, carrying the image information, is transferred to the second-order coherence of the down-converted field. Direct intensity measurements do not reveal information about the encoded object; only coincidence measurements do.

In addition, the system proves to be flexible in terms of space requirements, as some distances can be compressed, and also in terms of resolution, as the latter can be fully monitored only by  $f$ . However, one drawback is that the EMCCD camera used here requires several hours to acquire the  $10^6$ – $10^7$  frames needed to reconstruct the correlation images. To address the issue, a potential solution is using a different single-photon camera technology, such as a time-stamping camera [36,37], which combines high resolution and speed. Another possibility is to increase the crystal length to enhance the photon pair flux. However, this would also limit the size of the object that can be encoded with our method, as the crystal length  $L$  essentially acts as an iris with a diameter  $1/L$  in the object plane. In that case, one would also need to adapt both the lens before the crystal and object size to accommodate this constraint, at the expense of spatial resolution.

While theoretically feasible, implementing our scheme with classically correlated sources, like engineered anti-correlated thermal light [38], would pose experimental challenges and yield inferior contrast and spatial resolution compared to our approach. Moreover, using entangled photons opens the door to more complex encoding schemes based on entanglement, where multiple images could be encoded in different optical planes, for example, by adding crystal engineering [4]. Capitalizing on the flexibility and experimental simplicity of the setup, this could subsequently enable the development of new imaging and encoding-decoding protocols for high dimensional quantum information processing. This could find some applications in quantum communication and cryptography.

**Acknowledgments**—H. D. acknowledges funding from the ERC Starting Grant (No. SQIMIC-101039375).

C. V. analyzed the data, designed and performed the experiments. C. V. and H. D. conceived the original idea, discussed the results, and contributed to the manuscript. H. D. supervised the project.

- [1] C. K. Hong and L. Mandel, Theory of parametric frequency down conversion of light, *Phys. Rev. A* **31**, 2409 (1985).
- [2] A. M. Brańczyk, A. Fedrizzi, T. M. Stace, T. C. Ralph, and A. G. White, Engineered optical nonlinearity for quantum light sources, *Opt. Express* **19**, 55 (2011).
- [3] A. Dosseva, Ł. Cincio, and A. M. Brańczyk, Shaping the joint spectrum of down-converted photons through optimized custom poling, *Phys. Rev. A* **93**, 013801 (2016).
- [4] O. Yesharim, S. Pearl, J. Foley-Comer, I. Juwiler, and A. Arie, Direct generation of spatially entangled qudits using quantum nonlinear optical holography, *Sci. Adv.* **9**, eade7968 (2023).
- [5] A. Valencia, A. Ceré, X. Shi, G. Molina-Terriza, and J. P. Torres, Shaping the waveform of entangled photons, *Phys. Rev. Lett.* **99**, 243601 (2007).
- [6] M. Hendrych, M. Micuda, and J. Torres, Tunable control of the frequency correlations of entangled photons, *Opt. Lett.* **32**, 2339 (2007).
- [7] A. Mair, A. Vaziri, G. Weihs, and A. Zeilinger, Entanglement of the orbital angular momentum states of photons, *Nature (London)* **412**, 313 (2001).
- [8] S. P. Walborn, A. N. de Oliveira, S. Pádua, and C. H. Monken, Multimode Hong-Ou-Mandel interference, *Phys. Rev. Lett.* **90**, 143601 (2003).
- [9] E. V. Kovalkov, I. B. Bobrov, S. S. Straupe, and S. P. Kulik, Spatial bell-state generation without transverse mode subspace postselection, *Phys. Rev. Lett.* **118**, 030503 (2017).
- [10] E. V. Kovalkov, S. S. Straupe, and S. P. Kulik, Quantum state engineering with twisted photons via adaptive shaping of the pump beam, *Phys. Rev. A* **98**, 060301(R) (2018).
- [11] A. D’Errico, F. Hufnagel, F. Miatto, M. Rezaee, and E. Karimi, Full-mode characterization of correlated photon pairs generated in spontaneous downconversion, *Opt. Lett.* **46**, 2388 (2021).
- [12] M. Jabir, N. Apurv Chaitanya, M. Mathew, and G. Samanta, Direct transfer of classical non-separable states into hybrid entangled two photon states, *Sci. Rep.* **7**, 7331 (2017).
- [13] N. Bornman, W. Tavares Buono, M. Lovemore, and A. Forbes, Optimal pump shaping for entanglement control in any countable basis, *Adv. Quantum Technol.* **4**, 2100066 (2021).
- [14] X. Qiu, D. Zhang, W. Zhang, and L. Chen, Structured-pump-enabled quantum pattern recognition, *Phys. Rev. Lett.* **122**, 123901 (2019).
- [15] M. Minozzi, S. Bonora, A. Sergienko, G. Vallone, and P. Villoresi, Optimization of two-photon wave function in parametric down conversion by adaptive optics control of the pump radiation, *Opt. Lett.* **38**, 489 (2013).
- [16] P. Boucher, H. Defienne, and S. Gigan, Engineering spatial correlations of entangled photon pairs by pump beam shaping, *Opt. Lett.* **46**, 4200 (2021).
- [17] O. Lib and Y. Bromberg, Spatially entangled airy photons, *Opt. Lett.* **45**, 1399 (2020).
- [18] H. Defienne and S. Gigan, Spatially entangled photon-pair generation using a partial spatially coherent pump beam, *Phys. Rev. A* **99**, 053831 (2019).
- [19] W. Zhang, R. Fickler, E. Giese, L. Chen, and R. W. Boyd, Influence of pump coherence on the generation of position-momentum entanglement in optical parametric down-conversion, *Opt. Express* **27**, 20745 (2019).
- [20] O. Lib, G. Hasson, and Y. Bromberg, Real-time shaping of entangled photons by classical control and feedback, *Sci. Adv.* **6**, eabb6298 (2020).
- [21] C. H. Monken, P. H. SoutoRibeiro, and S. Pádua, Transfer of angular spectrum and image formation in spontaneous parametric down-conversion, *Phys. Rev. A* **57**, 3123 (1998).
- [22] M. Unternährer, B. Bessire, L. Gasparini, M. Perenzoni, and A. Stefanov, Super-resolution quantum imaging at the Heisenberg limit, *Optica* **5**, 1150 (2018).
- [23] A. K. Jha and R. W. Boyd, Spatial two-photon coherence of the entangled field produced by down-conversion using a partially spatially coherent pump beam, *Phys. Rev. A* **81**, 013828 (2010).
- [24] See Supplemental Material at <http://link.aps.org/supplemental/10.1103/PhysRevLett.133.093601> for more details, which includes Refs. [25–32].
- [25] H. Defienne, M. Reichert, and J. W. Fleischer, General model of photon-pair detection with an image sensor, *Phys. Rev. Lett.* **120**, 203604 (2018).
- [26] I. Yamaguchi and T. Zhang, Phase-shifting digital holography, *Opt. Lett.* **22**, 1268 (1997).
- [27] R. Camphausen, Á. Cuevas, L. Duempelmann, R. A. Terborg, E. Wajs, S. Tisa, A. Ruggeri, I. Cusini, F. Steinlechner, and V. Pruneri, A quantum-enhanced wide-field phase imager, *Sci. Adv.* **7**, eabj2155 (2021).
- [28] H. Defienne, P. Cameron, B. Ndagano, A. Lyons, M. Reichert, J. Zhao, A. R. Harvey, E. Charbon, J. W. Fleischer, and D. Faccio, Pixel super-resolution with spatially entangled photons, *Nat. Commun.* **13**, 3566 (2022).
- [29] A. F. Abouraddy, B. E. A. Saleh, A. V. Sergienko, and M. C. Teich, Entangled-photon Fourier optics, *J. Opt. Soc. Am. B* **19**, 1174 (2002).
- [30] P.-A. Moreau, J. Mougín-Sisini, F. Devaux, and E. Lantz, Realization of the purely spatial Einstein-Podolsky-Rosen paradox in full-field images of spontaneous parametric down-conversion, *Phys. Rev. A* **86**, 010101(R) (2012).
- [31] M. P. Edgar, D. S. Tasca, F. Izdebski, R. E. Warburton, J. Leach, M. Agnew, G. S. Buller, R. W. Boyd, and M. J. Padgett, Imaging high-dimensional spatial entanglement with a camera, *Nat. Commun.* **3**, 984 (2012).
- [32] M. Reichert, H. Defienne, and J. W. Fleischer, Optimizing the signal-to-noise ratio of biphoton distribution measurements, *Phys. Rev. A* **98**, 013841 (2018).
- [33] G. Ortolano, A. Paniate, P. Boucher, C. Napoli, S. Soman, S. F. Pereira, I. Ruo-Berchera, and M. Genovese, Quantum enhanced non-interferometric quantitative phase imaging, *Light* **12**, 171 (2023).
- [34] D. Zia, N. Dehghan, A. D’Errico, F. Sciarrino, and E. Karimi, Interferometric imaging of amplitude and phase of spatial biphoton states, *Nat. Photonics* **17**, 1009 (2023).

- [35] S. P. Walborn, C. Monken, S. Pádua, and P. S. Ribeiro, Spatial correlations in parametric down-conversion, *Phys. Rep.* **495**, 87 (2010).
- [36] A. Nomerotski, Imaging and time stamping of photons with nanosecond resolution in timepix based optical cameras, *Nucl. Instrum. Methods Phys. Res., Sect. A* **937**, 26 (2019).
- [37] V. Vidyapin, Y. Zhang, D. England, and B. Sussman, Characterisation of a single photon event camera for quantum imaging, *Sci. Rep.* **13**, 1009 (2023).
- [38] D. Venkatraman, N.D. Hardy, F.N. Wong, and J.H. Shapiro, Classical far-field phase-sensitive ghost imaging, *Opt. Lett.* **36**, 3684 (2011).